Title

Evaluation of non-modified wireframe DNA origami for acute toxicity and biodistribution in mice

Authors

Wamhoff, Eike-Christian[1]*, Knappe, Grant A.[1,2]*, Burds, Aurora A.[3], Du, Rebecca R.[1], Neun, Barry W.[4], Difilippantonio, Simone[5], Sanders, Chelsea[5], Edmondson, Elijah F.[6], Matta, Jennifer L.[6], Dobrovolskaia, Marina A.[4] and Bathe, Mark[1]**

[1]Department of Biological Engineering, Massachusetts Institute of Technology, Cambridge, MA 02139, United States of America

[2]Department of Chemical Engineering, Massachusetts Institute of Technology, Cambridge, MA 02139, United States of America

[3]Koch Institute for Integrative Cancer Research, Massachusetts Institute of Technology, Cambridge, MA 02139, United States of America

[4]Nanotechnology Characterization Laboratory, Cancer Research Technology Program, Frederick National Laboratory for Cancer Research, Frederick, MD 21702, United States of America

[5]Laboratory of Animal Sciences Program, Frederick National Laboratory for Cancer Research, Frederick, MD 21702, United States of America

[6]Molecular Histology and Pathology Laboratory, Frederick National Laboratory for Cancer Research, Frederick, MD 21702, United States of America

*These authors contributed equally

**Address correspondence to mark.bathe@mit.edu

Keywords

DNA origami; nanotechnology; toxicity; immunotoxicity; biodistribution; therapeutic delivery

Abstract

Wireframe DNA origami can be used to fabricate virus-like particles for a range of biomedical applications, including the delivery of nucleic acid therapeutics. However, the acute toxicity and biodistribution of these wireframe nucleic acid nanoparticles (NANPs) have not previously been characterized in animal models. In the present study, we observed no indications of toxicity in BALB/c mice following therapeutically relevant dosage of unmodified DNA-based NANPs via intravenous administration, based on liver and kidney histology, liver biochemistry, and body weight. Further, the immunotoxicity of these NANPs was minimal, as indicated by blood cell counts and type-I interferon and pro-inflammatory cytokines. In an SJL/J model of autoimmunity, we observed no indications of NANP-mediated DNA-specific antibody response or immune-mediated kidney pathology following the intraperitoneal administration of NANPs. Finally, biodistribution studies revealed that these NANPs accumulate in the liver within one hour, concomitant with substantial renal clearance. Our observations support the continued development of wireframe DNA-based NANPs as next-generation nucleic acid therapeutic delivery platforms.

Introduction

DNA nanostructures have been extensively explored in biomedical applications[1-3], and have emerged as a promising delivery platform for vaccines[4-6], nucleic acid therapeutics[7-10], and small molecule drugs[11-13]. The DNA origami method can produce monodisperse DNA-based nucleic acid nanoparticles (NANPs) on the 10-100 nm length scale with near-quantitative yields[14]. Compared with other nanoparticle (NP) delivery platforms, NANPs have several unique advantages[3, 15]. Independent control over the size and geometry of NANPs with site-specific functionalization may improve tissue- and cell-specific targeting[16], and their sequence-based programmability can be leveraged for logic-gated, controlled cargo release[17, 18]. NANPs have tunable biodegradation profiles[19], and can be modified chemically and structurally to control immunostimulation[4, 20, 21]. Additionally, NANPs can simply incorporate combinatorial ratios of nucleic acid therapeutics including siRNAs and CRISPR-RNPs through nucleic acid hybridization[15].

Two major classes of DNA origami have been developed to date: dense brick-like[22-24] and porous wireframe[25-27] architectures. Comparatively, wireframe NANPs require less nucleic acid for fabrication of similar size objects, which might lead to less immunostimulation, and additionally are stable in physiological buffers[19, 28]. Employing top-down design algorithms, wireframe NANPs

can be rapidly prototyped in both two[29-33] and three dimensions[28, 32-35]. Fully scalable production methods of single-stranded DNA 'scaffolds' with programmable sequence and length now enable preclinical and clinical biomedical applications for both classes of DNA origami[36-40].

DNA-based NANPs are biodegradable via endogenous nucleases, most notably DNase I extracellularly[19, 41]. This limits their potential cardio and pulmonary toxicity, which is associated with other nanoparticles[42], although this characteristic can also limit *in vivo* circulation times[19, 41, 43]. Two of the three major toxicity mechanisms of NPs, namely reactive oxygen species generation and release of metal ions, are not relevant for NANPs. Immunotoxicity has emerged as the third major toxicity type. Notably, both single- and double-stranded DNA (ssDNA and dsDNA) are recognized by the immune system through pattern recognition receptors. ssDNA containing unmethylated cytosine-guanine dinucleotide (CpG) sequence motifs activates endosomal toll-like receptor 9 (TLR9) signaling, and dsDNA activates the cytosolic cyclic GMP-AMP synthase (cGAS)-stimulator of interferon genes (STING) pathway[44, 45]. Additionally, NLRP3, AIM2, and IFI16 are components of the inflammasome capable of recognizing ss- and dsDNA[45]. The induction of proinflammatory cytokines via these signaling pathways can potentially result in hypersensitivity reactions like cytokine storm and anaphylaxis[46, 47]. Furthermore, antibody responses against nuclear DNA and chromatin have been implicated in driving autoimmunity and the pathogenesis of systemic lupus erythematosus (SLE)[48]. Thus, the potential for immunostimulation and immunotoxicity is a major safety consideration for DNA origami in biomedical applications.

Yet, the immunotoxicity of DNA-based NANPs remains underexplored, particularly in animal models and for wireframe NANPs. Initial *in vitro* cell-based studies revealed context-dependent immunostimulation with examples of rod-like DNA origami being immunologically inert[49], contrasted by modest immune cell activation by rod-like[20] and wireframe DNA origami[21, 50]. Both TLR9 and the cGAS-STING pathways contributed to immune recognition[20, 21]. Additionally, immunostimulation can intentionally be enhanced by the multivalent display of specific immunostimulatory nucleic acids, both *in vitro*[21, 49] and *in vivo*[4]. To date, however, no indications of immunotoxicity have been observed in animal models, with studies exploring different NANP geometries and administration routes, namely intravenous (i.v.)[12, 18, 51, 52] and intraperitoneal (i.p.)[52]. NANPs dosed below 1 mg/kg were reported to be immunologically inert[12, 18, 51] while more therapeutically relevant doses induced modest immunostimulation[52, 53] (for reference, therapeutic nucleic acids are typically dosed at 1-10 mg/kg clinically[54]). Several studies additionally evaluated the NANP-mediated induction of total and DNA-specific antibody responses[6, 52, 55] (i.e., immunogenicity). While total IgM levels transiently increased, no indications

91 of DNA-specific immunological memory or autoimmunity were observed. In contrast to brick-like
92 NANPs, the immunotoxicity and immunogenicity of wireframe NANPs have not been
93 characterized at therapeutically relevant doses in animal models.

94 In addition to preclinical safety profiles, characterizing the biodistribution is essential for
95 biomedical applications. Several brick-like DNA origami biodistribution studies have been
96 conducted[10, 12, 18, 50-52], exploring various shapes, routes of administration, and both healthy as
97 well as tumor-bearing mouse models. Again, the biodistribution of wireframe DNA origami
98 remains underexplored. One study investigated the biodistribution of a wireframe NANP with six
99 helices per edge after i.v. administration in C57 nude mice, and observed rapid bladder
100 accumulation and an elimination half-life under one hour[50].

101 Here, we characterize the acute toxicity and biodistribution of wireframe DNA-based
102 NANPs following i.v. and i.p. administration. In BALB/c mice at 4 mg/kg doses, we found no
103 phenotype across animal body weight, liver and kidney histology, and liver biochemistry.
104 Additionally, we observed no phenotype in immune blood cell counts, and minimal cytokine
105 induction. In SJL/J mice, commonly used as a model of autoimmunity, i.p. administration of
106 NANPs did not induce DNA-specific IgM or IgG antibody production; consequently, immune
107 complex-mediated kidney damage was also not observed. Finally, upon i.v. administration of
108 these NANPs, we observed accumulation in the liver within one hour, accompanied by rapid renal
109 clearance, as anticipated for biodegradable nanomaterials[56, 57]. Taken together, our study
110 suggests that wireframe DNA origami have limited immunotoxicity and accumulate in the liver,
111 supporting their continued development for biomedical applications including both liver-targeting
112 of nucleic acid therapeutics and also addressing the grand challenge of engineering these
113 materials for extrahepatic delivery.

114 Results

115 We designed and conducted a set of animal model experiments to investigate the biodistribution,
116 acute toxicity, and, specifically, immunotoxicity of wireframe NANPs (**Figure 1.A**). We
117 administered 4 mg/kg NANP i.v. into BALB/c mice and investigated toxicity readouts including
118 body weights, liver and kidney histology, liver and kidney biochemistry, blood cell counts, and
119 cytokine induction. Additionally, we administered 0.4 mg/kg NANP into SJL/J female mice i.p. to
120 understand the potential for wireframe NANPs to break immunological tolerance to self-DNA and
121 induce an autoimmune response. Finally, we administered 2 mg/kg of fluorophore-labeled NANP
122 into BALB/c mice i.v. to characterize their biodistribution. Taken together, these experiments

123 provided a baseline characterization of wireframe NANP toxicity and biodistribution at
124 therapeutically relevant doses.

125 We designed and fabricated a pentagonal bipyramid with 84 base pairs and two DNA
126 duplexes per edge (**PB84**) to serve as a model to assess the immunotoxicity and biodistribution
127 of wireframe NANPs (**Figure 1.B** and **S1**). Characterizing **PB84** by agarose gel electrophoresis,
128 dynamic light scattering, and atomic force microscopy, we observed monodisperse
129 nanostructures with an approximate diameter of 40 nm, which we were able to prepare in
130 milligram quantities for subsequent *in vivo* experiments.

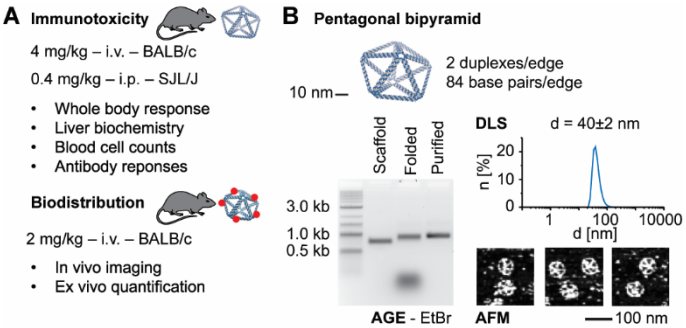

131
132 **Figure 1. Characterizing the acute toxicity and biodistribution of wireframe DNA origami**

133 **(A)** The experimental design for this study investigated the acute toxicity, immunotoxicity and biodistribution of
134 wireframe NANPs across two different animal models via two different administration routes. **(B)** The model NANP, a
135 pentagonal bipyramid with two duplexes and 84 base pairs per edge (**PB84**), used in this study. **PB84** structural integrity
136 was validated by agarose gel electrophoresis (AGE), dynamic light scattering (DLS), and atomic force microscopy
137 (AFM).
138

139 We first administered 4 mg/kg of **PB84** i.v. in at least four female BALB/c mice for each monitored
140 toxicity readout. Monitoring animal body weights over seven days after administration, no weight
141 loss was observed, comparable to PBS and unstructured ssDNA controls (**Figure 2.A**). Next, we
142 examined liver and kidney histology, noting that these two organs were the major sites of
143 accumulation observed in previous DNA origami studies[12, 18, 50-52]. We observed no indications of
144 pathology in the liver and kidney (**Figure 2.B**). We assayed liver and kidney biochemistry after
145 administration of **PB84** and observed no phenotype for the following biomarkers for toxicity:
146 alkaline phosphatase, aspartate aminotransferase, alanine aminotransferase, blood urea
147 nitrogen, creatinine, total serum protein, albumin, globulin, glucose, and bilirubin (**Figure 2.C**).

148 Next, we investigated whether NANP administration resulted in the proliferation of blood
149 cell types. No phenotype for abnormal cell counts was observed for total white blood cells, as well
150 as for lymphocytes and monocytes individually (**Figure 3** and **S2**). In addition to blood cell counts,
151 we investigated whether cytokines were produced following **PB84** administration, as they have
152 been implicated in NP and nucleic acid immunotoxicity[42, 47]. We conducted an enzyme-linked
153 immunoassay (ELISA) with serum from blood drawn at 3 and 24 hours after administration,

reflecting differential kinetics of cytokine induction (**Table 1**). We observed IL-6 and CXCL2 induction at 3 hours, and IL-12 and TNF induction at 24 hours, although these cytokine levels were not significantly increased compared to the PBS control.

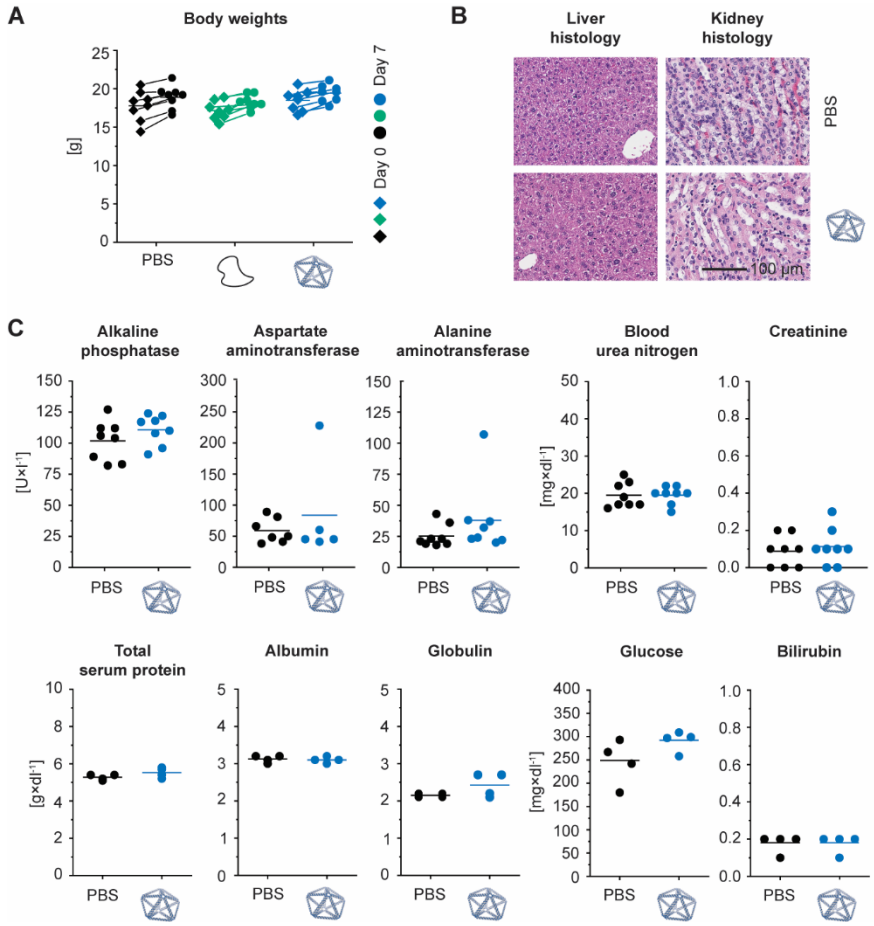

Figure 2. Effect of wireframe DNA origami on body weight as well as liver and kidney histology and function in BALB/c mice.

Intravenous administration of PB84 (4mg/kg), PBS control and an unstructured DNA control (4mg/kg). **(A)** Body weights were monitored before and seven days after administration. Body weight change was consistent across all groups. **(B)** Histological sections of kidney and liver were visualized by hematoxylin and eosin (H&E) staining and observed under a light microscope at 40× magnification. **(C)** A panel of 10 biomarkers for liver and kidney function shows no phenotype when NANPs were administered, consistent with a PBS control. General toxicity was assessed from n ≥ 4 biological replicates per group. Representative histology images are shown. Student's t-test was performed for the body weights. One-way ANOVA was performed for the liver and kidney biochemistry panel followed by Tukey's multiple comparison test. Significant differences are denoted as * - $p < 0.050$, ** - $p < 0.010$, and *** - $p < 0.001$.

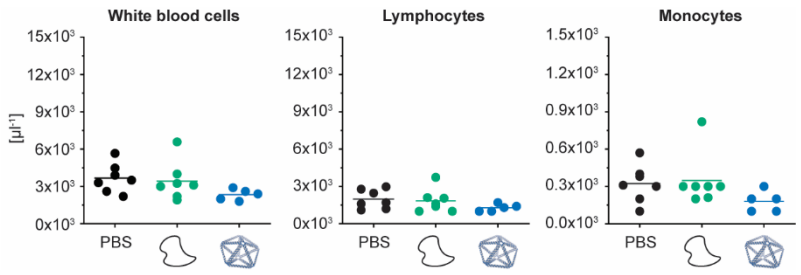

170 **Figure 3. Characterizing blood cell counts in BALB/c mice after i.v. administration**

171 BALB/c mice were intravenously administrated through tail-vein injection with 4 mg/kg of **PB84** per animal. Total white
172 blood cell, lymphocyte, and monocyte cell counts were not elevated when NANPs were administered, consistent with
173 a PBS control and an unstructured ssDNA control. Blood cell counts were assessed from n ≥ 5 biological replicates per
174 group. One-way ANOVA was performed for the blood cell counts followed by Tukey's multiple comparison test.
175 Significant differences are denoted as * - p < 0.050, ** - p < 0.010, and *** - p < 0.001.
176

177 **Table 1. Cytokine levels in BALB/c mice after i.v. administration**

178 A cytokine array panel was conducted at 3 and 24 hours after administration. PBS, **PB84**, and lipopolysaccharide (LPS)
179 were administrated i.v., and serum was collected at corresponding time points. Cytokine induction was assessed from
180 n = 3 biological replicates per group. Cytokine induction compared to PBS is shown. One-way ANOVA was performed
181 for the 3 h and 24 h time point followed by Tukey's multiple comparison test. Significant differences compared to PBS
182 are denoted as * - p < 0.050, ** - p < 0.010, and *** - p < 0.001.

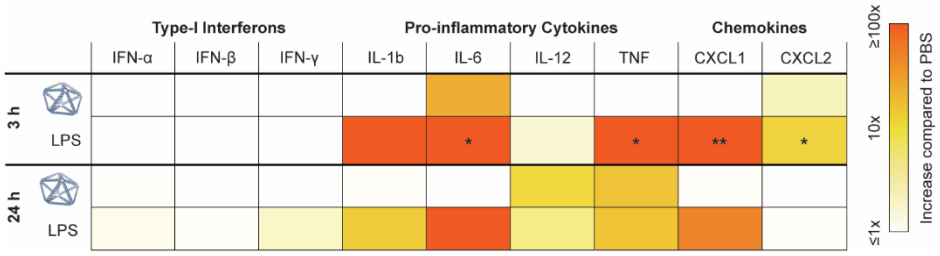

183
184

185 Next, to evaluate the potential of NANPs to break immunological tolerance to self-antigens and
186 induce an autoimmune response, we investigated their safety profiles in the SJL/J mouse model.
187 This mouse model is genetically predisposed to develop autoimmunity and is commonly used to
188 study chemically induced autoimmunity[58]. Female SJL/J mice have greater mortality and show
189 greater blood levels of DNA-specific antibodies and, subsequently, immune complex-mediated
190 kidney damage than male mice. This phenomenon is similar to SLE in humans, in which the male-
191 to-female disease incidence ratio is 1-to-9, and the disease is more severe in females. Therefore,
192 female mice were used in our study. We injected 0.4 mg/kg of **PB84** i.p. and observed no
193 significant phenotype when assessing kidney histology via a kidney score when compared with a
194 PBS control (**Figure 4.A** and **S3**). In contrast, all animals treated with pristane, used as a positive
195 control, showed histological changes characteristic of immune complex-mediated kidney
196 damage. We additionally monitored the production of DNA-specific IgM and IgG antibodies over
197 20 weeks (**Figure 4.B**). Unlike pristane, **PB84** did not induce DNA-specific IgM and IgG
198 production.

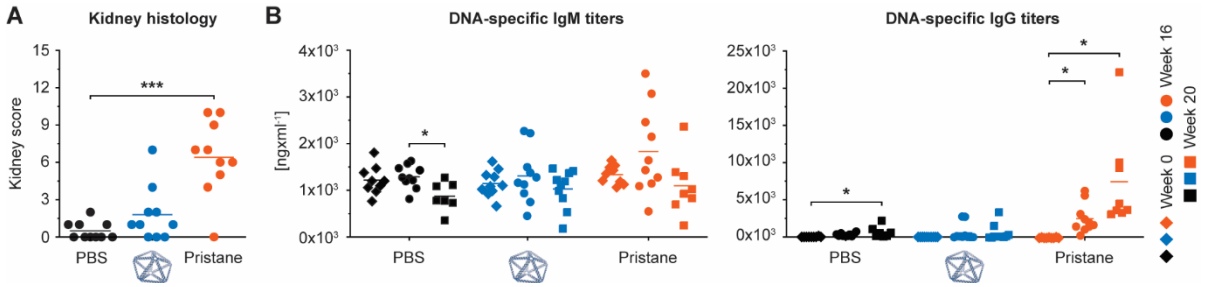

Figure 4. Characterizing autoimmunity induction in SJL/J mice after i.p. administration

SJL/J mice were intraperitoneally administered with 0.4 mg/kg of **PB84** per animal. **(A)** Kidney scores were assessed at 20 weeks post treatment and **(B)** DNA-specific IgM and IgG antibody titers were assessed before treatment (time 0 or baseline) and after 16- and 20-weeks post treatment from ten animals (n = 10) per group. One-way ANOVA was performed followed by Tukey's multiple comparison test. Significant differences are denoted as * - $p < 0.050$, ** - $p < 0.010$, and *** - $p < 0.001$.

Given that **PB84** was generally safe in different animal models and via different modes of administration, we sought to further understand this nanomaterial's potential as a delivery vehicle. Towards this end, we conducted a baseline biodistribution study of **PB84**. To facilitate *in vivo* and *ex vivo* characterization of **PB84**'s biodistribution, we installed 5 Alexa Fluor 750 fluorophores via pre-assembly functionalization to yield **PB84-5xAF750**. Following i.v. administration at 2 mg/kg**,** **PB84-5xAF750**'s biodistribution was monitored for several hours (**Figure 5.A** and **S4**) by *in vivo* imaging and organ accumulation was characterized *ex vivo* after 60 minutes (**Figure 5.B** and **S5**). Within 15 minutes, **PB84-5xAF750** was rapidly cleared from circulation as measured by blood draws (**Figure 5.C**), where it mainly accumulated in the liver (**Figure 5.A** and **S4.B**) and remained for at least two hours as renal clearance initiated. Importantly, this biodistribution profile was different than a fluorophore-labelled, control oligonucleotide, which was renally cleared within 15 minutes, with substantially less accumulation in the liver. *Ex vivo* imaging of harvested organs confirmed that **PB84-5xAF750** mainly accumulates in the liver after 60 minutes, with minor accumulation in the spleen, kidney, and lung (**Figure 5.B** and **S5**).

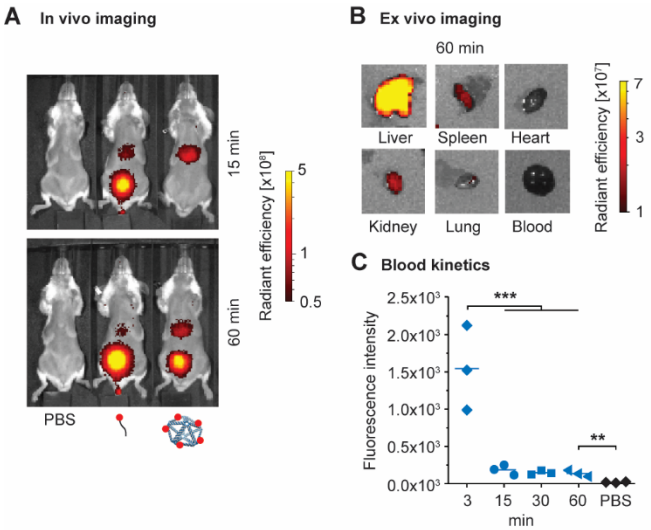

Figure 5. Biodistribution in BALB/c mice after i.v. administration

In vivo optical imaging for analysis of pharmacokinetics and biodistribution. BALB/c mice were injected with PBS, AlexaFluor750-labeled oligonucleotide, or a DNA origami **PB84-5xAF750** and imaged at multiple timepoints post-injection. **(A)** Representative fluorescence images at 15- and 60-minutes post-injection (n=3 per group). **(B)** Representative fluorescence images of ex vivo organs harvested 60 minutes post-injection of **PB84-5xAF750**. **PB84-5xAF750** was mostly accumulated in the liver, with minor accumulation in the kidney, spleen, and lung after 60 minutes. **(C)** Fluorescence intensity measurements of drawn blood for up to 60-minutes post-injection. One-way ANOVA was performed for blood kinetics measurements followed by Tukey's multiple comparison test. Significant differences are denoted as * - $p < 0.050$, ** - $p < 0.010$, and *** - $p < 0.001$.

Discussion

Overall, these data indicate that unmodified wireframe DNA-based NANPs are not acutely toxic after a single i.v. administration of therapeutically relevant doses, and NANPs accumulate in the liver prior to biodegradation and renal clearance. Unlike earlier studies with antisense DNA oligonucleotides which reported mononuclear cell infiltration in the liver and kidney[59], our general toxicity study did not reveal any kidney or liver damage as indicated by histology. We did not observe any phenotypes when assessing liver and kidney biochemistry, suggesting that NANPs do not alter the healthy functioning of the liver, even though this is their primary site of accumulation. We observed no change in the absolute globulin levels and albumin-globulin ratios. This indicates there was no onset of hypergammaglobulinemia, a pathology characterized by the over-production of globulin proteins by B cells, which is a characteristic response to antisense DNA oligonucleotides[59]. Monocytosis, another phenotype linked with antisense DNA oligonucleotides[59], was not observed either. This is in contrast to a previous study[52] in which transient monocytosis was observed for brick-like NANPs (12 mg/kg, i.p. administration, five repeat doses), which might be due to differential cell-specific uptake by these dense objects compared with the porous wireframe architecture explored here[60].

247 Importantly, mouse models generally serve as conservative estimates for immune cell
248 proliferation, such as monocytosis and splenomegaly, in response to nucleic acid therapeutics.
249 Only when tested in animals genetically predisposed to autoimmunity (SJL/J females), NANPs
250 resulted in grade 3 spleen plasmacytosis in one of ten animals (data not shown); since one animal
251 with grade 2 plasmacytosis was also detected in the PBS negative control group (data not shown),
252 this observation suggests that the risk of increase in the number of immune cells in response to
253 NANPs is low.

254 Since cytokine induction has been implicated in nanomaterial toxicity[42, 47], this innate
255 immune response was important to characterize. Three hours after administration, we observed
256 IL-6 and CXCL2 induction, and at 24 hours, we observed IL-12 and TNF induction; this induction
257 was not significantly higher than in the PBS control. Similar mild immunostimulation has been
258 observed in other DNA origami studies[52, 53]. DNA-induced TLR-9 signaling can lead to the
259 production of IL-6, IL-12, and TNF[45]. However, while TLRs have often been implicated in nucleic
260 acid therapeutic immunostimulation, they are often not the only source[59]. Further studies are
261 required to mechanistically determine the origins of the observed cytokine production. We note
262 that for some applications, such as cancer immunotherapy, the ability to stimulate
263 proinflammatory cytokine production might be a preferable characteristic of a delivery vehicle.
264 Researchers have demonstrated proof-of-concepts that immune system stimulation can be
265 programmed with NANPs[4, 20, 21, 49]. We anticipate this capability will be important in future
266 biomedical applications.

267 One potential safety concern relevant to the *in vivo* use of DNA-based NANPs is breaking
268 the immunological tolerance to DNA and inducing autoimmune responses via the generation of
269 DNA-specific antibodies. While no ideal preclinical model for autoimmunity studies is currently
270 available, SJL/J mice are commonly used to model the development of chemically-induced SLE,
271 an autoimmune condition characterized by broad self-reactive antibody responses and
272 glomerulonephritis[58]. We found that, unlike pristane, used as a positive control, NANPs do not
273 induce SLE phenotype in the SJL/J model, as assessed by kidney histology and DNA-specific
274 IgM and IgG serum levels. These data corroborate additional findings that DNA origami generally
275 does not elicit DNA-specific immunological memory[6, 52, 55]. We note that further understanding the
276 adaptive immune response against NANPs at different doses, dosing regimens, and routes of
277 administration will be important to further validate these findings. NANPs co-formulated with
278 peptides and proteins may also alter these adaptive immune responses.

279 A preliminary biodistribution study revealed that these wireframe NANPs rapidly exit the
280 bloodstream on the order of minutes, mainly accumulating in the liver at 60 minutes post-

281 administration. At 4 hours (**Figure S4.B**), the NANPs were cleared from the liver, suggesting that
282 the NANPs are biodegrading in the liver or bloodstream into fragmented NPs or oligonucleotides
283 that can then be processed by the renal system. This biodistribution is consistent with previous
284 studies on brick-like NANPs that found the liver as a major site of accumulation for NANPs[12, 18,
285 50, 52], as well as numerous studies of different classes of NPs due to the drastic reduction in hepatic
286 blood flow velocity and fenestrated cellular environment[56]. In a notable exception, researchers
287 observed that the kidney was the main organ of accumulation for larger (~100 nm characteristic
288 length scale) NANPs[51]. Additionally, the biodistribution of DNA origami can be altered when
289 NANPs are functionalized with biomacromolecules[43, 50]. Taken together, these data suggest that
290 the biodistribution of wireframe DNA-based NANPs may also be programmed by modulating the
291 size and shape of the NP, as well as the chemical composition and surface display of molecules.
292 Overall, these data support the continued development of wireframe DNA origami for
293 biomedical applications. Future investigations could explore various additional directions.
294 Following up on this acute toxicity study, evaluating safety profiles when NANPs are administered
295 across multiple administration routes at increased (and repeated) doses will lead to a deeper
296 understanding of the potential therapeutic window of these nanomaterials. For example,
297 understanding the doses at which safety issues emerge between intravenous and subcutaneous
298 administration will help prioritize further development efforts. We found that upon intravenous
299 administration, NANPs accumulate in the liver. Modulating the size, shape, and surface display
300 of molecules on NANPs may lead to accumulation in extra-hepatic tissues, which is of high priority
301 in the biomedical delivery field. Finally, metabolic studies understanding the rate of biodegradation
302 and the fate of the degradation products are required for better understanding the safety profiles
303 of these NANPs, with and without stabilizing modifications that alter their nuclease-driven
304 biodegradation and may also alter cellular uptake and tissue-targeting properties.
305

306 ## Acknowledgements

307 E.-C.W., G.A.K., R.R.D., and M.B. were supported by NSF CCF-1564025, NSF DMREF CBET-
308 1729397, NIH R21-EB026008, NIH R01-MH112694, ONR N00014-17-1-2609, ARO ISN
309 W911NF-13-D-0001, and FastGrant AGMT EFF 4/15/20. E.-C.W. was additionally supported by
310 the Feodor Lynen Fellowship of the Alexander von Humboldt Foundation. G.A.K. was additionally
311 supported by the National Science Foundation under a Graduate Research Fellowship 2389237.
312 This work made use of the MRSEC Shared Experimental Facilities at MIT, supported by NSF
313 DMR-1419807. Additional support for this research was provided by a core center grant P30-

ES002109 from the National Institute of Environmental Health Sciences, National Institutes of Health. We thank the Koch Institute's Robert A. Swanson (1969) Biotechnology Center (SBC) for technical support, specifically the Preclinical Imaging & Testing Facility, the Nanotechnology Materials Facility, and the Histology Facility. We also thank the MIT DCM Comparative Pathology Laboratory. A.A.B and the SBC are supported in part by the Koch Institute Support (core) Grant P30-CA14051 from the NCI. This study was funded in part (B.W.N., M.A.D., E.F.E., and J.L.M.) by federal funds from the National Cancer Institute, National Institutes of Health, under contract 75N91019D00024. The content of this publication does not necessarily reflect the views or policies of the Department of Health and Human Services, nor does mention of trade names, commercial products, or organizations imply endorsement by the US Government.

Methods

Materials and Equipment

All materials were purchased from Millipore Sigma, unless otherwise stated. Alexa Fluor 750-NHS was purchased from ThermoFisher Scientific. Nuclease-free water and oligonucleotide staples were purchased from IDT. Agarose was purchased from IBI Scientific. Black 96-well plates were purchased from Nunc. Tris-EDTA (TE), tris-acetate-EDTA (TAE) and phosphate-buffer saline (PBS) were purchased from Corning. The DNA ladder (Quick-Load Purple 2-log DNA ladder 0.1-10 kb) was purchased from New England Biolabs. ToxinSensor Gel Clot Endotoxin Assay Kits were purchased from GenScript. VacciGrade LPS was purchased from InvivoGen.

BioRad T100 Thermal Cyclers were used for DNA nanoparticle assembly. Agarose gels were imaged on a Typhoon FLA 7000. Agarose gel images were processed using ImageJ. DNA concentration measurements were made using a NanoDrop 2000 by ThermoFisher Scientific. Atomic force microscopy (AFM) was conducted using a Veeco Multimode 8 with ScanAsyst-Fluid+ tips. AFM images were processed using ImageJ. Dynamic light scattering (DLS) was performed using a Zetasizer Nano ZSP by Malvern Analytical. Purified oligonucleotides were dried *in vacuo* using a SpeedVac SPD300-DDA by ThermoFisher Scientific. Reversed-phase high-performance liquid chromatography (RP-HPLC) was conducted using a BEH C18 column by Waters. Alfalfa-free mouse diet was purchased from LabDiet. Imaging of live mice and harvested organs was performed using a Caliper Spectrum IVIS and images were process using Living Image Software by PerkinElmer.

346 **Scaffold and oligonucleotide staple synthesis**

347 The custom-length DNA scaffold (phPB84, 2520 nt) for **PB84** was prepared as previously
348 described[36]. Triton X-144 was used to remove residual endotoxins[43]. Endotoxin levels were
349 measured using ToxinSensor Gel Clot Endotoxin Assay Kits.

350 To install dyes onto oligonucleotide staples for our biodistribution studies, 50 μM staples
351 containing a 5' amino groups (IDT's C6 amino modifier) in PBS at pH 7.4 were reacted with 10x
352 excess of Alexa Fluor 750-NHS dissolved in DMSO overnight at room temperature. Subsequently,
353 excess dye was removed using NAP-10 columns and Alexa Fluor 750-modified staples were
354 purified via RP-HPLC (gradient: 90% 0.1% TEAA and 10% acetonitrile to 10% TEAA and 90%
355 acetonitrile over 30 min). Solvents were removed under vacuum and Alexa Fluor 750-modified
356 staples were dissolved in TE for further use.

357

358 **DNA nanoparticle design and assembly**

359 **PB84** and **PB84-5xAF750** were designed using DAEDALUS with the five dyes pointing into the
360 interior of the NANP from the base edges (**Tables S1-S3**)[28]. **PB84** and **PB84-5xAF750** were
361 assembled as previously described[28]. Briefly, a folding reaction containing 30 nM scaffold, 225
362 nM oligonucleotide staples, 1x TAE, 12 mM $MgCl_2$ was prepared in nuclease-free water. The
363 reaction mixture was dispensed into 50 μl aliquots and then subjected to the following thermal
364 annealing treatment: 95 °C for 5 min, 80-75 °C at 1 °C per 5 min, 75-30 °C at 1 °C per 15 min,
365 and 30-25 °C at 1 °C per 10 min. The reaction mixture was then purified into PBS using Amicon
366 Ultra centrifugal filters (100 kDa, 2000 G, 3x, 20 minutes) and stored at 4 °C. Purity and dispersity
367 of resulting NANPs were characterized by agarose gel electrophoresis (1.6 wt% agarose, TAE 12
368 mM $MgCl_2$ buffer, EtBr stain, 65V for 150 minutes at 4 °C) as well as dynamic light scattering.
369 Endotoxin levels were measured using ToxinSensor Gel Clot Endotoxin Assay Kits to ensure
370 administration of less than 5 EU/kg.

371

372 **Atomic force microscopy**

373 AFM imaging was performed in TAE with 12 mM $MgCl_2$ at pH 8.3 using ScanAsyst mode and
374 ScanAsyst-Fluid tips. Following the deposition of 5 μl **PB84-5xAF750** at 5 nM in PBS at pH 7.4
375 onto freshly cleaved mica, 2 μl $NiCl_2$ at 100 mM were added and incubated for 30 s. Subsequently,
376 80 μl of TAE with 12 mM $MgCl_2$ at pH 8.3 were added to the sample and the AFM tip was
377 submerged into 40 μl TAE with 12 mM $MgCl_2$ at pH 8.3 before starting the experiment.

378

379 **Animals**

380 Genetically inbred *wild type* male and female BALB/cJ (strain 000651) and female SJL/J (strain
381 000686) mice were purchased from The Jackson Laboratory (Bar Harbor, ME), and were housed
382 and handled in Association for Assessment and Accreditation of Laboratory Animal Care
383 (AAALAC)-accredited facilities with experimental methods as specifically approved by the
384 Institutional Animal Care and Use Committees at MIT and NCI-Frederick, respectively.

385

386 **Gross toxicity, histology, and liver and kidney biochemistry panel in BALB/c model**

387 BALB/c mice received a single 100 µl intravenous tail vein injection consisting of PBS, 4mg/kg
388 unstructured phPB84 scaffold in PBS, or 4mg/kg **PB84** in PBS. Animals were monitored daily for
389 one week. Blood was collected via cardiac puncture to obtain whole blood counts within an hour
390 of collection as well as serum for chemistry panel to assay liver and kidney function (IDEXX
391 BioAnalytics, Columbia, MO). Necropsy was performed to look for signs of gross toxicity. For
392 histologic evaluation, formalin-fixed tissues were embedded in paraffin, sectioned at 5 µm, stained
393 with hematoxylin and eosin (H&E), and visually assessed under a microscope by a veterinary
394 pathologist.

395

396 **Cytokine array in BALB/c mice**

397 Cardiac blood was collected from BALB/c mice 3 hr and 24 hr after tail vein injection of 100 µL
398 containing PBS, **PB84** (4mg/kg) in PBS, or immunogenic lipopolysaccharide (LPS 0.05mg/mL).
399 Serum was stored at -80°C before shipment for analysis of induction of cytokines via a custom
400 murine Q-Plex array (Quansys Biosciences). The custom array included IFN-α, IFN-β, IFN-γ, IL-
401 1b, IL-6, IL-12, TNF, CXCL1 and CXCL2.

402

403 **Biodistribution studies in BALB/c mice**

404 Prior to biodistribution studies, mice were kept on an alfalfa free diet (LabDiet, AIN-93M, cat#
405 58M1, irradiated) for 7 days to reduce background fluorescence. BALB/c mice received a single
406 100ul intravenous tail vein injection consisting of PBS, 2mg/kg oligonucleotide staple-AF750 in
407 PBS, or 2mg/kg DNA origami PB84-5xAF750 in PBS. Live mice were anesthetized with 2%
408 isoflurane and imaged immediately after injection and 15 min, 30 min, 45 min, 1 hr, 2 hr, 4 hr, and
409 6 hr post-injection. Peripheral blood was collected immediately after injection and 15 min, 30 min,
410 45 min, and 60 min post-injection, then transferred to a 96-well plate for measurement of the
411 fluorescent signal. For ex vivo imaging of liver, kidney, heart, spleen, and lungs, mice were
412 euthanized via CO_2 1 hr post-injection and organs were harvested.

413

414 **Autoimmunity study in SJL/J model**

415 Eight weeks old SJL/J females were injected intraperitoneally with 500 μL of either negative
416 control (PBS), positive control (pristane at stock concentration as provided by Sigma Aldrich,
417 catalog # P9622) or 0.4 mg/kg **PB84**. Pristane was synthetic, certified for in vivo studies, having
418 > 95% purity by GC and undetectable endotoxin (< 5EU/mL). Average mouse weight at the time
419 of injection was 19 g. Each treatment group included 10 animals. The blood was collected before
420 injection (baseline) and at 8, 16, and 20 weeks post-injection. Sera were analyzed by ELISA for
421 the presence of anti-dsDNA IgG and IgM using commercially available kits (Chondrex Inc.,
422 catalog #3031 and #3032, respectively). At the termination of the study, kidneys were collected,
423 fixed in 4% neutral buffered formalin and stained with Periodic Acid–Schiff (PAS) reagent for
424 detection of immune complex depositions and with hematoxylin and eosin (H&E) for
425 characterization of histologic lesions. Histopathology grading was based on the most severe
426 kidney section for each animal. Grading was performed for glomerular changes, inflammatory
427 infiltrates, and tubular changes as follows: 0 – normal; 1 – minimal; 2 – mild; 3 – moderate; 4 –
428 marked. Inflammatory infiltrates were graded as 0, within normal limits; 1, minimally increased
429 inflammatory infiltrates composed predominantly of lymphocytes and plasma cells often focally
430 forming 3-5 cell thick perivascular cuffs; 2, mildly increased inflammatory infiltrates that are
431 multifocal; 3, moderately increased inflammatory infiltrates that form thick perivascular cuffs
432 multifocally that are prominent with the 4x objective; 4, markedly increased inflammatory infiltrates
433 that widely separate vessels from adjacent renal parenchyma. Tubular changes were graded as
434 follows: 0, within normal limits; 1, minimal tubular degeneration often focal; 2, mild tubular
435 degeneration present with multifocal regions containing tubular degeneration and regeneration
436 and focal necrosis; 3, moderate tubular changes contain tubular degeneration and multifocal
437 necrosis; 4, marked tubular changes including tubular necrosis multifocally. Mesangial expansion
438 was evaluated and graded into four categories: 0, no mesangial expansion; 1, minimal changes;
439 2, mild mesangial expansion (mesangial matrix wide < 2 nucleus diameter); 3, moderate
440 mesangial expansion often with crescentic glomeruli, mesangial matrix wide < 4 nucleus
441 diameter), and 4, severe mesangial expansion (> 4 nucleus diameter). Cumulative score was
442 calculated and reported as “kidney score”.

443

Supplemental Information

Additional AFM data; Additional blood cell count data; SJL/J model histology images; Additional in vivo imaging; Additional ex vivo imaging; Scaffold and staple sequences; Raw data for cytokine panel.

References

1. Bujold, K. E.; Lacroix, A.; Sleiman, H. F., DNA Nanostructures at the Interface with Biology. *Chem* **2018,** *4* (3), 495-521.

2. He, L.; Mu, J.; Gang, O.; Chen, X., Rationally Programming Nanomaterials with DNA for Biomedical Applications. *Adv Sci* **2021,** *8* (8), 2003775.

3. Afonin, K. A.; Dobrovolskaia, M. A.; Church, G.; Bathe, M., Opportunities, Barriers, and a Strategy for Overcoming Translational Challenges to Therapeutic Nucleic Acid Nanotechnology. *ACS Nano* **2020,** *14* (8), 9221-9227.

4. Liu, S.; Jiang, Q.; Zhao, X.; Zhao, R.; Wang, Y.; Wang, Y.; Liu, J.; Shang, Y.; Zhao, S.; Wu, T.; Zhang, Y.; Nie, G.; Ding, B., A DNA nanodevice-based vaccine for cancer immunotherapy. *Nat Mater* **2021,** *20* (3), 421-430.

5. Veneziano, R.; Moyer, T. J.; Stone, M. B.; Wamhoff, E. C.; Read, B. J.; Mukherjee, S.; Shepherd, T. R.; Das, J.; Schief, W. R.; Irvine, D. J.; Bathe, M., Role of nanoscale antigen organization on B-cell activation probed using DNA origami. *Nat Nanotechnol* **2020,** *15* (8), 716-723.

6. Wamhoff, E.-C.; Ronsard, L.; Feldman, J.; Hauser, B. M.; Knappe, G. A.; Romanov, A.; Lam, E.; St. Denis, K.; Balazs, A. B.; Schmidt, A.; Lingwood, D.; Bathe, M., Enhancing antibody responses by multivalent antigen display on thymus-independent DNA origami scaffolds. *bioRxiv* **2022**, 2022.08.16.504128.

7. Bujold, K. E.; Hsu, J. C. C.; Sleiman, H. F., Optimized DNA "Nanosuitcases" for Encapsulation and Conditional Release of siRNA. *J Am Chem Soc* **2016,** *138* (42), 14030-14038.

8. Wang, Z.; Song, L.; Liu, Q.; Tian, R.; Shang, Y.; Liu, F.; Liu, S.; Zhao, S.; Han, Z.; Sun, J.; Jiang, Q.; Ding, B., A Tubular DNA Nanodevice as a siRNA/Chemo-Drug Co-delivery Vehicle for Combined Cancer Therapy. *Angew Chem Int Ed Engl* **2021,** *60* (5), 2594-2598.

9. Lin-Shiao, E.; Pfeifer, W. G.; Shy, B. R.; Saffari Doost, M.; Chen, E.; Vykunta, V. S.; Hamilton, J. R.; Stahl, E. C.; Lopez, D. M.; Sandoval Espinoza, C. R.; Deyanov, A. E.; Lew, R. J.; Poirer, M. G.; Marson, A.; Castro, C. E.; Doudna, J. A., CRISPR-Cas9-mediated nuclear transport and genomic integration of nanostructured genes in human primary cells. *Nucleic Acids Res* **2022,** *50* (3), 1256-1268.

10. Liu, J.; Song, L.; Liu, S.; Jiang, Q.; Liu, Q.; Li, N.; Wang, Z. G.; Ding, B., A DNA-Based Nanocarrier for Efficient Gene Delivery and Combined Cancer Therapy. *Nano Lett* **2018,** *18* (6), 3328-3334.

480 11. Wiraja, C.; Zhu, Y.; Lio, D. C. S.; Yeo, D. C.; Xie, M.; Fang, W.; Li, Q.; Zheng, M.;
481 Van Steensel, M.; Wang, L.; Fan, C.; Xu, C., Framework nucleic acids as programmable carrier
482 for transdermal drug delivery. *Nat Commun* **2019,** *10* (1), 1147.

483 12. Zhang, Q.; Jiang, Q.; Li, N.; Dai, L.; Liu, Q.; Song, L.; Wang, J.; Li, Y.; Tian, J.; Ding,
484 B.; Du, Y., DNA origami as an in vivo drug delivery vehicle for cancer therapy. *ACS Nano* **2014,**
485 *8* (7), 6633-43.

486 13. Kim, K. R.; Kang, S. J.; Lee, A. Y.; Hwang, D.; Park, M.; Park, H.; Kim, S.; Hur, K.;
487 Chung, H. S.; Mao, C.; Ahn, D. R., Highly tumor-specific DNA nanostructures discovered by in
488 vivo screening of a nucleic acid cage library and their applications in tumor-targeted drug delivery.
489 *Biomaterials* **2019,** *195*, 1-12.

490 14. Rothemund, P. W., Folding DNA to create nanoscale shapes and patterns. *Nature* **2006,**
491 *440* (7082), 297-302.

492 15. Dobrovoskaia, M. A.; Bathe, M., Opportunities and challenges for the clinical translation
493 of structuredDNAassemblies as gene therapeutic delivery and vaccine vectors. *Wiley*
494 *Interdisciplinary Reviews-Nanomedicine and Nanobiotechnology* **2021,** *13* (1), e1657.

495 16. Knappe, G. A.; Wamhoff, E. C.; Bathe, M., Functionalizing DNA origami to investigate
496 and interact with biological systems. *Nat Rev Mater* **2023,** *8*, 123-138.

497 17. Douglas, S. M.; Bachelet, I.; Church, G. M., A logic-gated nanorobot for targeted transport
498 of molecular payloads. *Science* **2012,** *335* (6070), 831-4.

499 18. Li, S.; Jiang, Q.; Liu, S.; Zhang, Y.; Tian, Y.; Song, C.; Wang, J.; Zou, Y.; Anderson,
500 G. J.; Han, J. Y.; Chang, Y.; Liu, Y.; Zhang, C.; Chen, L.; Zhou, G.; Nie, G.; Yan, H.; Ding,
501 B.; Zhao, Y., A DNA nanorobot functions as a cancer therapeutic in response to a molecular
502 trigger in vivo. *Nat Biotechnol* **2018,** *36*, 258-264.

503 19. Chandrasekaran, A. R., Nuclease resistance of DNA nanostructures. *Nat Rev Chem* **2021,**
504 *5* (4), 225-239.

505 20. Schuller, V. J.; Heidegger, S.; Sandholzer, N.; Nickels, P. C.; Suhartha, N. A.; Endres,
506 S.; Bourquin, C.; Liedl, T., Cellular immunostimulation by CpG-sequence-coated DNA origami
507 structures. *ACS Nano* **2011,** *5* (12), 9696-702.

508 21. Du, R. R.; Cedrone, E.; Romanov, A.; Falkovich, R.; Dobrovolskaia, M. A.; Bathe, M.,
509 Innate Immune Stimulation Using 3D Wireframe DNA Origami. *ACS Nano* **2022,** *16* (12), 20340-
510 20352.

511 22. Douglas, S. M.; Dietz, H.; Liedl, T.; Hogberg, B.; Graf, F.; Shih, W. M., Self-assembly
512 of DNA into nanoscale three-dimensional shapes. *Nature* **2009,** *459* (7245), 414-8.

513 23. Dietz, H.; Douglas, S. M.; Shih, W. M., Folding DNA into twisted and curved nanoscale
514 shapes. *Science* **2009,** *325* (5941), 725-30.

515 24. Castro, C. E.; Kilchherr, F.; Kim, D. N.; Shiao, E. L.; Wauer, T.; Wortmann, P.; Bathe,
516 M.; Dietz, H., A primer to scaffolded DNA origami. *Nat Methods* **2011,** *8* (3), 221-9.

517 25. Zhang, F.; Jiang, S.; Wu, S.; Li, Y.; Mao, C.; Liu, Y.; Yan, H., Complex wireframe DNA
518 origami nanostructures with multi-arm junction vertices. *Nat Nanotechnol* **2015,** *10* (9), 779-84.

519 26. Shih, W. M.; Quispe, J. D.; Joyce, G. F., A 1.7-kilobase single-stranded DNA that folds
520 into a nanoscale octahedron. *Nature* **2004,** *427* (6975), 618-21.

521 27. Hong, F.; Jiang, S.; Wang, T.; Liu, Y.; Yan, H., 3D Framework DNA Origami with Layered
522 Crossovers. *Angew Chem Int Ed Engl* **2016,** *55* (41), 12832-5.

523 28. Veneziano, R.; Ratanalert, S.; Zhang, K.; Zhang, F.; Yan, H.; Chiu, W.; Bathe, M.,
524 Designer nanoscale DNA assemblies programmed from the top down. *Science* **2016,** *352* (6293),
525 1534.

526 29. Benson, E.; Mohammed, A.; Bosco, A.; Teixeira, A. I.; Orponen, P.; Hogberg, B.,
527 Computer-Aided Production of Scaffolded DNA Nanostructures from Flat Sheet Meshes. *Angew*
528 *Chem Int Ed Engl* **2016,** *55* (31), 8869-72.

529 30. Jun, H.; Zhang, F.; Shepherd, T.; Ratanalert, S.; Qi, X.; Yan, H.; Bathe, M.,
530 Autonomously designed free-form 2D DNA origami. *Sci Adv* **2019,** *5* (1), eaav0655.

531 31. Jun, H.; Wang, X.; Bricker, W. P.; Bathe, M., Automated sequence design of 2D
532 wireframe DNA origami with honeycomb edges. *Nat Commun* **2019,** *10* (1), 5419.

533 32. Huang, C. M.; Kucinic, A.; Johnson, J. A.; Su, H. J.; Castro, C. E., Integrated computer-
534 aided engineering and design for DNA assemblies. *Nat Mater* **2021,** *20* (9), 1264-1271.

535 33. Jun, H.; Wang, X.; Parsons, M. F.; Bricker, W. P.; John, T.; Li, S.; Jackson, S.; Chiu,
536 W.; Bathe, M., Rapid prototyping of arbitrary 2D and 3D wireframe DNA origami. *Nucleic Acids*
537 *Res* **2021,** *49* (18), 10265-10274.

538 34. Jun, H.; Shepherd, T. R.; Zhang, K.; Bricker, W. P.; Li, S.; Chiu, W.; Bathe, M.,
539 Automated Sequence Design of 3D Polyhedral Wireframe DNA Origami with Honeycomb Edges.
540 *ACS Nano* **2019,** *13* (2), 2083-2093.

541 35. Benson, E.; Mohammed, A.; Gardell, J.; Masich, S.; Czeizler, E.; Orponen, P.; Hogberg,
542 B., DNA rendering of polyhedral meshes at the nanoscale. *Nature* **2015,** *523* (7561), 441-4.

543 36. Shepherd, T. R.; Du, R. R.; Huang, H.; Wamhoff, E.-C.; Bathe, M., Bioproduction of
544 pure, kilobase-scale single-stranded DNA. *Sci Rep* **2019,** *9* (1), 6121.

545 37. Praetorius, F.; Kick, B.; Behler, K. L.; Honemann, M. N.; Weuster-Botz, D.; Dietz, H.,
546 Biotechnological mass production of DNA origami. *Nature* **2017,** *552* (7683), 84-87.

547 38. Nafisi, P. M.; Aksel, T.; Douglas, S. M., Construction of a novel phagemid to produce
548 custom DNA origami scaffolds. *Synth Biol* **2018,** *3* (1).

549 39. Engelhardt, F. A. S.; Praetorius, F.; Wachauf, C. H.; Bruggenthies, G.; Kohler, F.; Kick,
550 B.; Kadletz, K. L.; Pham, P. N.; Behler, K. L.; Gerling, T.; Dietz, H., Custom-Size, Functional,
551 and Durable DNA Origami with Design-Specific Scaffolds. *ACS Nano* **2019,** *13* (5), 5015-5027.

552 40. Minev, D.; Guerra, R.; Kishi, J. Y.; Smith, C.; Krieg, E.; Said, K.; Hornick, A.; Sasaki,
553 H. M.; Filsinger, G.; Beliveau, B. J.; Yin, P.; Church, G. M.; Shih, W. M., Rapid in vitro production
554 of single-stranded DNA. *Nucleic Acids Res* **2019,** *47* (22), 11956-11962.

555 41. Wamhoff, E. C.; Romanov, A.; Huang, H.; Read, B. J.; Ginsburg, E.; Knappe, G. A.;
556 Kim, H. M.; Farrell, N. P.; Irvine, D. J.; Bathe, M., Controlling Nuclease Degradation of Wireframe
557 DNA Origami with Minor Groove Binders. *ACS Nano* **2022,** *16* (6), 8954-8966.

558 42. Yang, W.; Wang, L.; Mettenbrink, E. M.; DeAngelis, P. L.; Wilhelm, S., Nanoparticle
559 Toxicology. *Annu Rev Pharmacol Toxicol* **2021,** *61*, 269-289.

560 43. Ponnuswamy, N.; Bastings, M. M. C.; Nathwani, B.; Ryu, J. H.; Chou, L. Y. T.; Vinther,
561 M.; Li, W. A.; Anastassacos, F. M.; Mooney, D. J.; Shih, W. M., Oligolysine-based coating
562 protects DNA nanostructures from low-salt denaturation and nuclease degradation. *Nat Commun*
563 **2017,** *8*, 15654.

564 44. Hornung, V., SnapShot: nucleic acid immune sensors, part 1. *Immunity* **2014,** *41* (5), 868,
565 868 e1.

566 45. Hornung, V., SnapShot: Nucleic acid immune sensors, part 2. *Immunity* **2014,** *41* (6),
567 1066-1066 e1.

568 46. Dobrovolskaia, M. A.; Shurin, M.; Shvedova, A. A., Current understanding of interactions
569 between nanoparticles and the immune system. *Toxicol Appl Pharmacol* **2016,** *299*, 78-89.

570 47. Elsabahy, M.; Wooley, K. L., Cytokines as biomarkers of nanoparticle immunotoxicity.
571 *Chem Soc Rev* **2013,** *42* (12), 5552-76.

572 48. Sisirak, V.; Sally, B.; D'Agati, V.; Martinez-Ortiz, W.; Ozcakar, Z. B.; David, J.;
573 Rashidfarrokhi, A.; Yeste, A.; Panea, C.; Chida, A. S.; Bogunovic, M.; Ivanov, II; Quintana, F.
574 J.; Sanz, I.; Elkon, K. B.; Tekin, M.; Yalcinkaya, F.; Cardozo, T. J.; Clancy, R. M.; Buyon, J.
575 P.; Reizis, B., Digestion of Chromatin in Apoptotic Cell Microparticles Prevents Autoimmunity. *Cell*
576 **2016,** *166* (1), 88-101.

577 49. Comberlato, A.; Koga, M. M.; Nussing, S.; Parish, I. A.; Bastings, M. M. C., Spatially
578 Controlled Activation of Toll-like Receptor 9 with DNA-Based Nanomaterials. *Nano Lett* **2022,** *22*
579 (6), 2506-2513.

580 50. Perrault, S. D.; Shih, W. M., Virus-inspired membrane encapsulation of DNA
581 nanostructures to achieve in vivo stability. *ACS Nano* **2014,** *8* (5), 5132-40.

582 51. Jiang, D.; Ge, Z.; Im, H. J.; England, C. G.; Ni, D.; Hou, J.; Zhang, L.; Kutyreff, C. J.;
583 Yan, Y.; Liu, Y.; Cho, S. Y.; Engle, J. W.; Shi, J.; Huang, P.; Fan, C.; Yan, H.; Cai, W., DNA
584 origami nanostructures can exhibit preferential renal uptake and alleviate acute kidney injury. *Nat*
585 *Biomed Eng* **2018,** *2* (11), 865-877.

586 52. Lucas, C. R.; Halley, P. D.; Chowdury, A. A.; Harrington, B. K.; Beaver, L.;
587 Lapalombella, R.; Johnson, A. J.; Hertlein, E. K.; Phelps, M. A.; Byrd, J. C.; Castro, C. E., DNA
588 Origami Nanostructures Elicit Dose-Dependent Immunogenicity and Are Nontoxic up to High
589 Doses In Vivo. *Small* **2022,** *18* (26), e2108063.

590 53. Palazzolo, S.; Hadla, M.; Spena, C. R.; Bayda, S.; Kumar, V.; Lo Re, F.; Adeel, M.;
591 Caligiuri, I.; Romano, F.; Corona, G.; Canzonieri, V.; Toffoli, G.; Rizzolio, F., Proof-of-Concept
592 Multistage Biomimetic Liposomal DNA Origami Nanosystem for the Remote Loading of
593 Doxorubicin. *ACS Med Chem Lett* **2019,** *10* (4), 517-521.

594 54. Kulkarni, J. A.; Witzigmann, D.; Thomson, S. B.; Chen, S.; Leavitt, B. R.; Cullis, P. R.;
595 van der Meel, R., The current landscape of nucleic acid therapeutics. *Nat Nanotechnol* **2021,** *16*
596 (6), 630-643.

597 55. Liu, X.; Xu, Y.; Yu, T.; Clifford, C.; Liu, Y.; Yan, H.; Chang, Y., A DNA nanostructure
598 platform for directed assembly of synthetic vaccines. *Nano Lett* **2012,** *12* (8), 4254-9.

599 56. Poon, W.; Kingston, B. R.; Ouyang, B.; Ngo, W.; Chan, W. C. W., A framework for
600 designing delivery systems. *Nat Nanotechnol* **2020,** *15* (10), 819-829.

601 57. Tsoi, K. M.; MacParland, S. A.; Ma, X. Z.; Spetzler, V. N.; Echeverri, J.; Ouyang, B.;
602 Fadel, S. M.; Sykes, E. A.; Goldaracena, N.; Kaths, J. M.; Conneely, J. B.; Alman, B. A.;
603 Selzner, M.; Ostrowski, M. A.; Adeyi, O. A.; Zilman, A.; McGilvray, I. D.; Chan, W. C.,
604 Mechanism of hard-nanomaterial clearance by the liver. *Nat Mater* **2016,** *15* (11), 1212-1221.

605 58. Satoh, M.; Richards, H. B.; Shaheen, V. M.; Yoshida, H.; Shaw, M.; Naim, J. O.;
606 Wooley, P. H.; Reeves, W. H., Widespread susceptibility among inbred mouse strains to the
607 induction of lupus autoantibodies by pristane. *Clin Exp Immunol* **2000,** *121* (2), 399-405.

608 59. Dobrovolskaia, M. A.; McNeil, S. E., Immunological and hematological toxicities
609 challenging clinical translation of nucleic acid-based therapeutics. *Expert Opin Biol Ther* **2015,** *15*
610 (7), 1023-48.

611 60. Wang, Y.; Benson, E.; Fordos, F.; Lolaico, M.; Baars, I.; Fang, T.; Teixeira, A. I.;
612 Hogberg, B., DNA Origami Penetration in Cell Spheroid Tissue Models is Enhanced by Wireframe
613 Design. *Adv Mater* **2021,** *33* (29), e2008457.

614